

## Dynamics of the equilibrium electrons in a helical-wiggler free-electron laser with reversed guide field

Shi-Chang Zhang

*China Center of Advanced Science and Technology (World Laboratory), P.O. Box 8730, Beijing, People's Republic of China and Department of Applied Physics, Southwest Jiaotong University, Chengdu, Sichuan 610031, People's Republic of China\**

Yong Xu and Qing-Xiang Liu<sup>†</sup>

*Department of Applied Physics, Southwest Jiaotong University, Chengdu, Sichuan 610031, People's Republic of China*  
(Received 14 December 1992; revised manuscript received 19 March 1993)

The dynamical behavior of a relativistic electron governed by the combination of a helical-wiggler magnetic field with a reversed guide magnetic field is investigated by generating Poincaré surface-of-section maps. The Hamiltonian description is derived in detail. It is found that the helical orbits are always stable. Computer simulation shows that the separatrix of the closed and open curves in phase portrait in this case is quite different from the one in the case of a positive guide field. An interesting effect numerically predicated is that increasing the self-field narrows the spread of longitudinal momentum. No chaos appears for the experimental parameters of Conde and Bekefi [Phys. Rev. Lett. **67**, 3082 (1991)], although the self-fields destroy the integrability of the motion.

PACS number(s): 41.60.Cr, 52.75.Ms, 42.52.+x, 05.45.+b

### I. INTRODUCTION

The free-electron laser (FEL) has been an active area of research due to its attractive properties, such as high efficiency, tunable frequency from microwave to x ray, and powerful output. High gain in free-electron-laser operation often requires intense beam current and an axial guide magnetic field. The dynamical behavior of the equilibrium electrons in a FEL is of importance because it not only is the basis of theoretical analysis but also practically determines whether the electron beam can be transported and efficiently interact with the electromagnetic wave. The helical orbits, as a special case, were first investigated by Frieland [1] in terms of the one-dimensional wiggler model. Then the calculation was extended to the three-dimensional wiggler by Freund, Johnston, and Sprangle [2], and recently the electrostatic and magnetostatic self-fields were taken into account by Zhang and Zhang [3,4]. In practice, however, not all equilibrium electrons have helical orbits. We have shown that the off-axis electrons cannot have helical orbits [5]. Considering that the self-fields destroy the integrability of the motion, several authors analyzed the chaotic behavior of the equilibrium electrons by generating Poincaré surface-of-section maps [6–10]. Upon improving the accuracy of numerical iterations, however, we found that the self-field-induced chaotic behavior seems not to be as serious as it was indicated before, and that, on the contrary, some open curves in the phase portrait become closed with increasing self-fields [11].

A recent experiment was reported by Conde and Bekefi [12], where the efficiency was dramatically raised from 2% up to 27% by using a reversed guide magnetic field. Several authors [13,14] attempted to give a theoretical explanation. In our opinion, the efficiency enhancement may result from two parts: one is that the quality of the

electron beam may be improved by a reversed guide field; the other is that there may be a new interaction mechanism between the beam and rf fields. We had a guesswork that the self-fields of the  $e$  beam may be a substantial factor in this kind of device [15]. As is well known, the self-fields of the  $e$  beam contain a dc part and a rf part. The latter is referred to as a space-charge wave. Recently, Freund and Ganguly [14] gave a numerical simulation by taking the lowest-order Gould-Trivelpiece mode into account. In the present paper we consider the effect of dc self-fields of the  $e$  beam by generating Poincaré maps. Our results will confirm the improvement of the beam quality. We concentrate the emphasis on the comparison with a positive guide field [6], and so a simplified model is employed when we give our Hamiltonian description.

We organize this paper as follows. In Sec. II a detailed Hamiltonian description is given for the equilibrium electrons in a free-electron laser with a reversed guide field, where the electrostatic and magnetostatic self-fields are taken into account. In Sec. III the phase portrait and helical orbits in the case of an integrable limit are analyzed. The effect of self-fields on the nonhelical orbits is numerically simulated by generating Poincaré surface-of-section maps in Sec. IV. Finally, brief conclusions are drawn in Sec. V.

### II. HAMILTONIAN DESCRIPTION AND NUMERICAL CALCULATION METHOD

#### A. Equations of motion

We consider a relativistic electron beam drifting in the field configuration consisting of a helical-wiggler magnetic field

$$\mathbf{B}_w = -B_w(\hat{\mathbf{e}}_x \cos k_w z + \hat{\mathbf{e}}_y \sin k_w z), \quad (1)$$

and a reversed guide magnetic field

$$\mathbf{B}_0 = -B_0 \hat{\mathbf{e}}_z, \quad (2)$$

where  $B_w$  and  $B_0$  are constant amplitudes,  $k_w$  is the wiggler wave number, and  $\hat{\mathbf{e}}_x$ ,  $\hat{\mathbf{e}}_y$ , and  $\hat{\mathbf{e}}_z$  are the unit vectors in  $x$ ,  $y$ , and  $z$  directions, respectively. Assume that the solid electron beam is cylindrical with radius  $r_b$ , axial velocity  $v_b \hat{\mathbf{e}}_z$ , and uniform density  $n_b$ . Within the beam the electrostatic and magnetostatic self-fields can be expressed as [16]

$$\mathbf{E}_s = -(m\omega_{pb}^2/2e)(x\hat{\mathbf{e}}_x + y\hat{\mathbf{e}}_y) \quad (3)$$

and

$$\mathbf{B}_s = (m\omega_{pb}^2\beta_b/2e)(y\hat{\mathbf{e}}_x - x\hat{\mathbf{e}}_y), \quad (4)$$

where  $-e$  and  $m$  are the electron charge and rest mass, respectively,  $\omega_{pb} = (4\pi e^2 n_b/m)^{1/2}$  is the nonrelativistic plasma frequency, and  $\beta_b = v_b/c$  is the normalized beam velocity divided by the light speed in vacuum  $c$ . The Hamiltonian of a test electron within the beam is

$$\begin{aligned} H &= [(c\mathbf{P} + e\mathbf{A})^2 + m^2c^4]^{1/2} - e\Phi_s \\ &\equiv \gamma mc^2 - e\Phi_s, \end{aligned} \quad (5)$$

where

$$\mathbf{A} = -B_0 x \hat{\mathbf{e}}_y + A_w(\hat{\mathbf{e}}_x \cos k_w z + \hat{\mathbf{e}}_y \sin k_w z) + \beta_b \Phi_s \hat{\mathbf{e}}_z \quad (6)$$

is the vector potential,

$$\Phi_s = (m\omega_{pb}^2/4e)(x^2 + y^2) \quad (7)$$

is the scalar potential,

$$\gamma = [1 + (\mathbf{p}/mc)^2]^{1/2} \quad (8)$$

is the relativistic energy factor,  $\mathbf{p} = \mathbf{P} + e\mathbf{A}/c$  is the mechanical momentum, and  $\mathbf{P}$  stands for the canonical momentum. Assuming  $B_0 \neq 0$ , we perform the canonical transformation  $(x, y, z, P_x, P_y, P_z) \rightarrow (\varphi, \psi, z', P_\varphi, P_\psi, P_{z'})$  as follows:

$$\begin{aligned} x &= \left[ \frac{2P_\varphi}{m\Omega_c} \right]^{1/2} \cos(\varphi - k_w z') \\ &\quad - \left[ \frac{2P_\psi}{m\Omega_c} \right]^{1/2} \sin(\psi + k_w z'), \end{aligned} \quad (9)$$

$$\begin{aligned} y &= \left[ \frac{2P_\psi}{m\Omega_c} \right]^{1/2} \cos(\psi + k_w z') \\ &\quad - \left[ \frac{2P_\varphi}{m\Omega_c} \right]^{1/2} \sin(\varphi - k_w z'), \end{aligned} \quad (10)$$

$$z = z', \quad (11)$$

$$P_x = -\sqrt{2m\Omega_c P_\varphi} \sin(\varphi - k_w z'), \quad (12)$$

$$P_y = -\sqrt{2m\Omega_c P_\psi} \sin(\psi + k_w z'), \quad (13)$$

$$P_z = P_{z'} + k_w P_\varphi - k_w P_\psi, \quad (14)$$

where  $\Omega_c = eB_0/mc$  represents the nonrelativistic cyclotron frequency. The Hamiltonian can be rewritten as

$$\begin{aligned} \hat{H}(\varphi, \psi, P_\varphi, P_\psi, P_{z'}) &= [1 + a_w^2 + 2\hat{\Omega}_c \hat{P}_\varphi \\ &\quad - 2a_w \sqrt{2\hat{\Omega}_c \hat{P}_\varphi} \sin\varphi \\ &\quad + (\hat{P}_{z'} + \hat{P}_\varphi - \hat{P}_\psi + \beta_b \hat{\Phi}_s)^2]^{1/2} - \hat{\Phi}_s \\ &\equiv \gamma - \hat{\Phi}_s, \end{aligned} \quad (15)$$

where

$$\hat{\Phi}_s(\varphi, \psi, \hat{P}_\varphi, \hat{P}_\psi) = 2\epsilon \hat{\Omega}_c [\hat{P}_\varphi + \hat{P}_\psi - 2\sqrt{\hat{P}_\varphi \hat{P}_\psi} \sin(\varphi + \psi)] \quad (16)$$

and

$$\epsilon = \omega_{pb}^2/4\Omega_c^2. \quad (17)$$

The dimensionless parameter  $\epsilon$  characterizes the strength of self-fields compared to the guide field. All the quantities are normalized by

$$\begin{aligned} \hat{\Omega}_c &= \frac{\Omega_c}{ck_w}, \quad \hat{\omega}_{pb} = \frac{\omega_{pb}}{ck_w}, \quad \hat{\Phi}_s = \frac{e\Phi_s}{mc^2}, \\ a_w &= \frac{eA_w}{mc^2}, \quad \hat{P}_{z'} = \frac{P_{z'}}{mc}, \quad \hat{P}_\varphi = \frac{k_w P_\varphi}{mc}, \\ \hat{P}_\psi &= \frac{k_w P_\psi}{mc}, \quad \hat{H} = \frac{H}{mc^2}, \quad \hat{z}' = k_w z'. \end{aligned} \quad (18)$$

It should be pointed out that although the above model is similar to the one in the case of a positive guide field [6], the Hamiltonian and the canonical transformation are different from each other.

Since the Hamiltonian  $\hat{H}(\varphi, \psi, \hat{P}_\varphi, \hat{P}_\psi, \hat{P}_{z'})$  does not explicitly contain  $z'$  and time  $t$ , we immediately obtain the constants of motion

$$\hat{P}_{z'} = \hat{P}_{z'0} = \text{const}, \quad (19)$$

$$\hat{H}(\varphi, \psi, \hat{P}_\varphi, \hat{P}_\psi, \hat{P}_{z'}) = \hat{H}_0 = \text{const}. \quad (20)$$

Consequently, the equations of motion become

$$\begin{aligned} \frac{d\varphi}{d\tau} &= \frac{\hat{P}_z}{\gamma} + \frac{\hat{\Omega}_c}{\gamma} \left[ 1 - \frac{a_w}{\sqrt{2\hat{\Omega}_c \hat{P}_\varphi}} \sin\varphi \right] \\ &\quad - 2\epsilon \hat{\Omega}_c \left[ 1 - \left[ \frac{\hat{P}_\psi}{\hat{P}_\varphi} \right]^{1/2} \sin(\varphi + \psi) \right] \left[ 1 - \beta_b \frac{\hat{P}_z}{\gamma} \right] \\ &\equiv f_1(\varphi, \psi, \hat{P}_\varphi, \hat{P}_\psi, \hat{P}_{z'}), \end{aligned} \quad (21)$$

$$\begin{aligned} \frac{d\hat{P}_\varphi}{d\tau} &= \frac{a_w}{\gamma} \sqrt{2\hat{\Omega}_c \hat{P}_\varphi} \cos\varphi \\ &\quad - 4\epsilon \hat{\Omega}_c \sqrt{\hat{P}_\varphi \hat{P}_\psi} \cos(\varphi + \psi) \left[ 1 - \beta_b \frac{\hat{P}_z}{\gamma} \right] \\ &\equiv f_2(\varphi, \psi, \hat{P}_\varphi, \hat{P}_\psi, \hat{P}_{z'}), \end{aligned} \quad (22)$$

$$\begin{aligned} \frac{d\psi}{d\tau} &= -\frac{\hat{p}_z}{\gamma} - 2\epsilon\hat{\Omega}_c \left[ 1 - \left[ \frac{\hat{p}_\varphi}{\hat{p}_\psi} \right]^{1/2} \sin(\varphi + \psi) \right] \\ &\quad \times \left[ 1 - \beta_b \frac{\hat{p}_z}{\gamma} \right] \\ &\equiv f_3(\varphi, \psi, \hat{p}_\varphi, \hat{p}_\psi, \hat{p}_{z'}) , \end{aligned} \quad (23)$$

$$\begin{aligned} \frac{d\hat{p}_\psi}{d\tau} &= -4\epsilon\hat{\Omega}_c \sqrt{\hat{p}_\varphi \hat{p}_\psi} \cos(\varphi + \psi) \left[ 1 - \beta_b \frac{\hat{p}_z}{\gamma} \right] \\ &\equiv f_4(\varphi, \psi, \hat{p}_\varphi, \hat{p}_\psi, \hat{p}_{z'}) , \end{aligned} \quad (24)$$

where  $\tau = ck_w t$  is the normalized time.

### B. Numerical calculation method

It is worthwhile to note that the normalized mechanical momentum defined by

$$\hat{p}_z = \hat{p}_{z'} + \hat{p}_\varphi - \hat{p}_\psi + \beta_b \hat{\Phi}_s , \quad (25)$$

the relativistic energy factor  $\gamma$ , and the normalized scalar potential  $\hat{\Phi}_s$  are functions of the canonical variables  $\varphi$ ,  $\psi$ ,  $\hat{p}_\varphi$ ,  $\hat{p}_\psi$ , and  $\hat{p}_{z'}$ . Substituting Eq. (19) into (20), we can easily find that among the four variables  $\varphi$ ,  $\psi$ ,  $\hat{p}_\varphi$ , and  $\hat{p}_\psi$ , only three are independent and one of them must be dependent, say,  $\hat{p}_\psi = \hat{p}_\psi(\varphi, \psi, \hat{p}_\varphi)$ . In principle therefore the problem can be solved by integrating these three differential equations, i.e., Eqs. (21)–(23), plus two algebraic equations (19) and (20). In this way, however, no invariant can be used to monitor the accuracy of iterations when we numerically integrate Eqs. (21)–(23). So we prefer to lay Eq. (19) aside and use the four differential equations, i.e., Eqs. (21)–(24), plus algebraic equation (20). That is, we iterate  $\varphi$ ,  $\psi$ ,  $\hat{p}_\varphi$ , and  $\hat{p}_\psi$  by numerically integrating Eqs. (21)–(24); then we derive  $\hat{p}_{z'}$  by substituting  $\varphi$ ,  $\psi$ ,  $\hat{p}_\varphi$ , and  $\hat{p}_\psi$  into Eq. (20). For each step of the iterations we compare  $\hat{p}_{z'}$  with its initial value  $\hat{p}_{z'0}$  in terms of Eq. (19). The smaller is the value of  $(\hat{p}_{z'} - \hat{p}_{z'0})$ , the more accurate are the numerical iterations. Poincaré surface-of-section maps can be generated for  $\psi = 0, \text{mod}(2\pi)$ . Furthermore, in order to ensure that the plots of the Poincaré maps exactly correspond to the sections of  $\psi = 0, \text{mod}(2\pi)$ , we rewrite Eqs. (21)–(24) as  $\psi$ -dependent forms:

$$\frac{d\varphi}{d\psi} = \frac{f_1}{f_3} , \quad (26)$$

$$\frac{d\hat{p}_\varphi}{d\psi} = \frac{f_2}{f_3} , \quad (27)$$

$$\frac{d\tau}{d\psi} = \frac{1}{f_3} , \quad (28)$$

$$\frac{d\hat{p}_\psi}{d\psi} = \frac{f_4}{f_3} , \quad (29)$$

and then let the iteration step of  $\psi$  be  $2\pi/N$ , where  $N$  is a sufficiently great integer. Thus the plots for  $\psi = 0, \text{mod}(2\pi)$  can be exactly collected on the  $(qN)$ th step ( $q = 0, 1, 2, 3, \dots$ ). Here one should bear it in mind that if

$\tau$  is negative in the iteration, one should use the following forms instead of Eqs. (26)–(29):

$$\frac{d\varphi}{d\psi'} = -\frac{f_1}{f_3} ,$$

$$\frac{d\hat{p}_\varphi}{d\psi'} = -\frac{f_2}{f_3} ,$$

$$\frac{d\tau}{d\psi'} = -\frac{1}{f_3} ,$$

$$\frac{d\hat{p}_\psi}{d\psi'} = -\frac{f_4}{f_3} ,$$

where  $\psi' = -\psi$ .

In this paper numerical integrating is programmed in FORTRAN77 computer language with double precision by using the Runge-Kutta method of order four. Calculations are carried out on a microcomputer (AST 386/33) with a mathematical co-processor. Similar to the situation of a positive guide field [6], Poincaré surface-of-section maps are performed by plane  $(\hat{p}_z, \varphi)$  instead of  $(\hat{p}_\varphi, \varphi)$  with the aid of Eq. (25).

In practice, there is an adiabatic range before the entrance of the wiggler in the free-electron laser. The initial states of the equilibrium electrons at the entrance of the wiggler are determined by the distribution of the adiabatic magnetic field. To coincide with the experiment, in this paper we have simulated the motion of the electrons in the adiabatic range by making use of the three-dimensional adiabatic distribution of Fig. 4 in Ref. [17]. The results are shown in Fig. 1, which are used as the parameters of the test electrons in the interaction range.

Using the numerical method mentioned above, we have successfully generated Poincaré maps in the case of a positive guide field [11]. We found that chaos appeared for group-II orbits when the iteration step of  $\psi$  was  $2\pi/650$ . But we immediately recognized from the information monitored by  $\hat{p}_{z'}$  that the result was doubtful because the relative error  $(\hat{p}_{z'} - \hat{p}_{z'0})/\hat{p}_{z'0}$  was not good enough. Upon changing the iteration step of  $\psi$  from  $2\pi/650$  to  $2\pi/6500$ , the computation-artifact chaos disappeared [11]. This shows that the self-fields are not serious enough to cause the chaos, although the integrability of motion is destroyed by these self-fields. We further found that in the case of the reversed guide field the iteration step should be shorter. In the present paper we choose the iteration step of  $\psi$  to be  $2\pi/65000$ , which keeps the relative error  $(\hat{p}_{z'} - \hat{p}_{z'0})/\hat{p}_{z'0}$  on the order of  $10^{-4}$ .

## III. ANALYSIS OF THE INTEGRABLE LIMIT

### A. Helical orbits and orbital stability

The equations of motion (21)–(24) are nonintegrable when the self-fields are taken into account (i.e.,  $\epsilon \neq 0$ ). In this section we analyze the dynamical behavior in the  $\epsilon = 0$  limit. Under this circumstance the Hamiltonian  $\hat{H}$  does not explicitly contain  $\psi$ . Thus there are three constants of motion:  $\hat{p}_{z'}$ ,  $\hat{H}$ , and  $\hat{p}_\psi$ . The dynamical system

becomes integrable. The equations of motion are reduced to two differential equations:

$$\frac{d\varphi}{d\tau} = \frac{\hat{p}_z}{\gamma} + \frac{\hat{\Omega}_c}{\gamma} \left[ 1 - \frac{a_w}{\sqrt{2\hat{\Omega}_c\hat{P}_\varphi}} \sin\varphi \right], \quad (30)$$

$$\frac{d\hat{P}_\varphi}{d\tau} = \frac{a_w}{\gamma} \sqrt{2\hat{\Omega}_c\hat{P}_\varphi} \cos\varphi. \quad (31)$$

A helical orbit corresponds to the fixed point of Eqs. (30) and (31). The parameters, denoted by subscript  $f$ , can be derived from  $d\varphi/d\tau=0$  and  $d\hat{P}_\varphi/d\tau=0$ , which satisfy the following relationship:

$$\cos\varphi_f = 0, \quad (32)$$

$$\sqrt{2\hat{\Omega}_c\hat{P}_{\varphi f}} = \pm \frac{a_w\hat{\Omega}_c}{\hat{p}_{zf} + \hat{\Omega}_c}.$$

Substituting Eq. (32) into (15), we rewrite the parameters of helical orbits as

$$\varphi_f = \frac{\pi}{2}, \quad (33)$$

$$\hat{p}_{zf}^2 \left[ 1 + \frac{a_w^2}{(\hat{p}_{zf} + \hat{\Omega}_c)^2} \right] + 1 = \gamma_f^2.$$

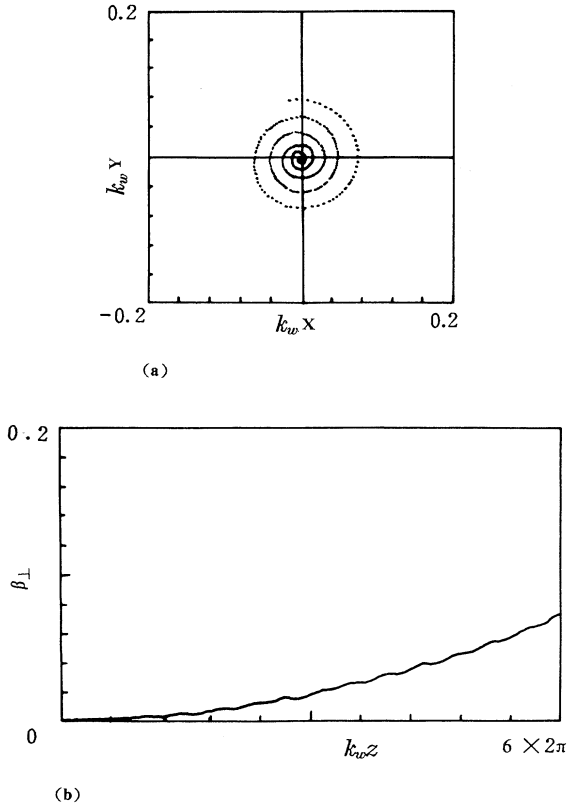


FIG. 1. Three-dimensional simulation of the test electron in the adiabatic range of the wiggler: (a) cross-sectional project of trajectory, and (b) normalized transverse velocity, where  $\gamma_0=2.4677$ ,  $a_w=0.4368$ ,  $\hat{\Omega}_c=3.2365$ ,  $(2\hat{P}_{\varphi 0}/\hat{\Omega}_c)^{1/2}=0.25$ , and  $\epsilon=0$ .

To examine the stability of helical orbits, we let

$$\varphi = \varphi_f + \delta\varphi, \quad |\delta\varphi| \ll \varphi_f, \quad (34)$$

$$\hat{P}_\varphi = \hat{P}_{\varphi f} + \delta\hat{P}_\varphi, \quad |\delta\hat{P}_\varphi| \ll \hat{P}_{\varphi f}.$$

Inserting Eq. (34) into (32) and making use of (33), we approximately obtain

$$\frac{d^2\delta\varphi}{d\tau^2} = - \left[ \frac{a_w}{\gamma_f^2} \sqrt{2\hat{\Omega}_c\hat{P}_{\varphi f}} \left[ \frac{a_w\hat{\Omega}_c}{2\hat{P}_{\varphi f}\sqrt{2\hat{\Omega}_c\hat{P}_{\varphi f}}} + 1 \right] \right] \delta\varphi. \quad (35)$$

Here we see that the helical orbits are always stable regardless of  $\hat{\Omega}_c > \hat{p}_z$  or  $\hat{\Omega}_c < \hat{p}_z$ , since the perturbed quantities are sine and cosine functions of  $\tau$ . This is quite different from the case of a positive guide field [1].

## B. Phase portrait

In the  $\epsilon=0$  limit the phase portrait is performed on the  $(\hat{p}_z, \varphi)$  plane by solving Eqs. (30) and (31). The numerical simulation is carried out for the reversed-guide-field FEL experiment [12], where  $B_0 = -10900$  G,  $B_w = 1470$  G,  $k_w = 2\pi/3.18$  cm $^{-1}$ ,  $\gamma = 2.4677$ , and  $r_b = 0.254$  cm. We choose the radial position of the test electron at the entrance  $r_g$  to be 0.127 cm. The corresponding normalized quantities are  $\hat{\Omega}_c = 3.2365$ ,  $a_w = 0.4368$ ,  $\hat{r}_b = 0.5$ , and  $\hat{r}_c \equiv (2P_{\psi 0}/\Omega_c)^{1/2} = 0.25$ . After simulating the motion of the test electron in the adiabatic range, we find that its gyroradius at the entrance of the wiggler,  $(2\hat{P}_{\varphi 0}/\hat{\Omega}_c)^{1/2}$ , is 0.074, and the axial normalized velocity  $\beta_b = 0.91$  (see Fig. 1).

Figure 2 shows the phase portraits for the four test electrons with  $\hat{r}_c = 0.074, 0.10, 0.16$ , and  $0.18$ , respectively, where  $\hat{r}_c \equiv (2\hat{P}_{\varphi 0}/\hat{\Omega}_c)^{1/2}$ . They respectively denote four kinds of curves: fixed point, closed curve, separatrix, and unbounded curve. From Fig. 2 we can find that the experimental parameter of Ref. [12],  $\hat{r}_c = 0.074$ , corresponds to the fixed point. Therefore most of the equilibrium electrons in the experiment of Ref. [12] had helical orbits, and the other equilibrium electrons had periodical orbits within the neighborhood of the helical orbits due to the small beam spread. Our calculations indicate that the phase curves for  $0.074 < \hat{r}_c < 0.16$  are closed and do not cross each other, and that the phase curves for  $\hat{r}_c > 0.16$  are unbounded and also do not cross each other. As shown in the figure, however, both closed curves and unbounded curves lie on the same side of the separatrix; consequently, an unbounded curve can cross a closed curve. This is very different from the circumstance of a positive guide field, where the unbounded curves lie on one side of the separatrix, and closed curves on the other side, and they do not cross each other. The reason that the phase curves cross in Fig. 2 is related to the mathematical property of Eqs. (30) and (31). In this paper we leave it alone because  $\hat{r}_c < 0.16$  was always satisfied in the experiment [12].

IV. INFLUENCE OF THE SELF-FIELDS ON POINCARÉ MAPS

In the preceding section we found that most of the equilibrium electrons in the experiment [12] had fixed-point phase portraits and that their orbits were therefore helical. On the other hand, some of the equilibrium electrons must have had non-fixed-point phase portraits due

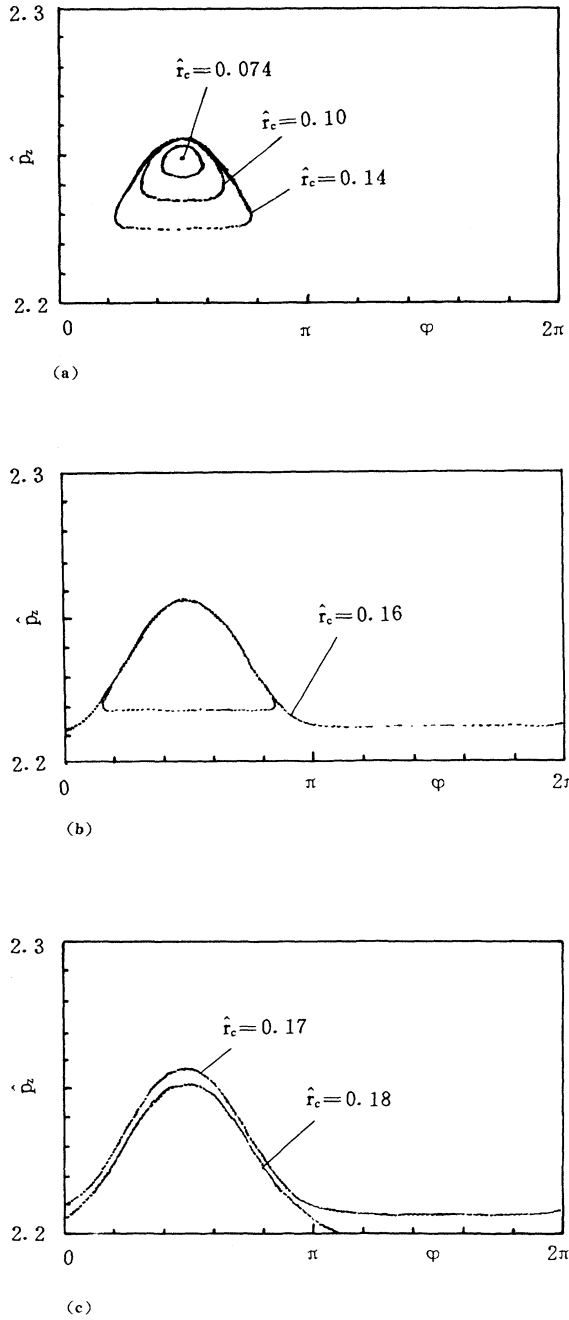


FIG. 2. Phase portrait of equilibrium electrons in a helical-wiggler free-electron laser with reversed guide magnetic field: (a) fixed-point and closed phase curves, (b) separatrix, and (c) open phase curves, where  $\gamma_0=2.4677$ ,  $a_w=0.4368$ ,  $\hat{\Omega}_c=3.2365$ ,  $(2\hat{P}_{\psi_0}/\hat{\Omega}_c)^{1/2}=0.25$ ,  $\epsilon=0$ , and  $\hat{r}_c$  is the initial gyroradius.

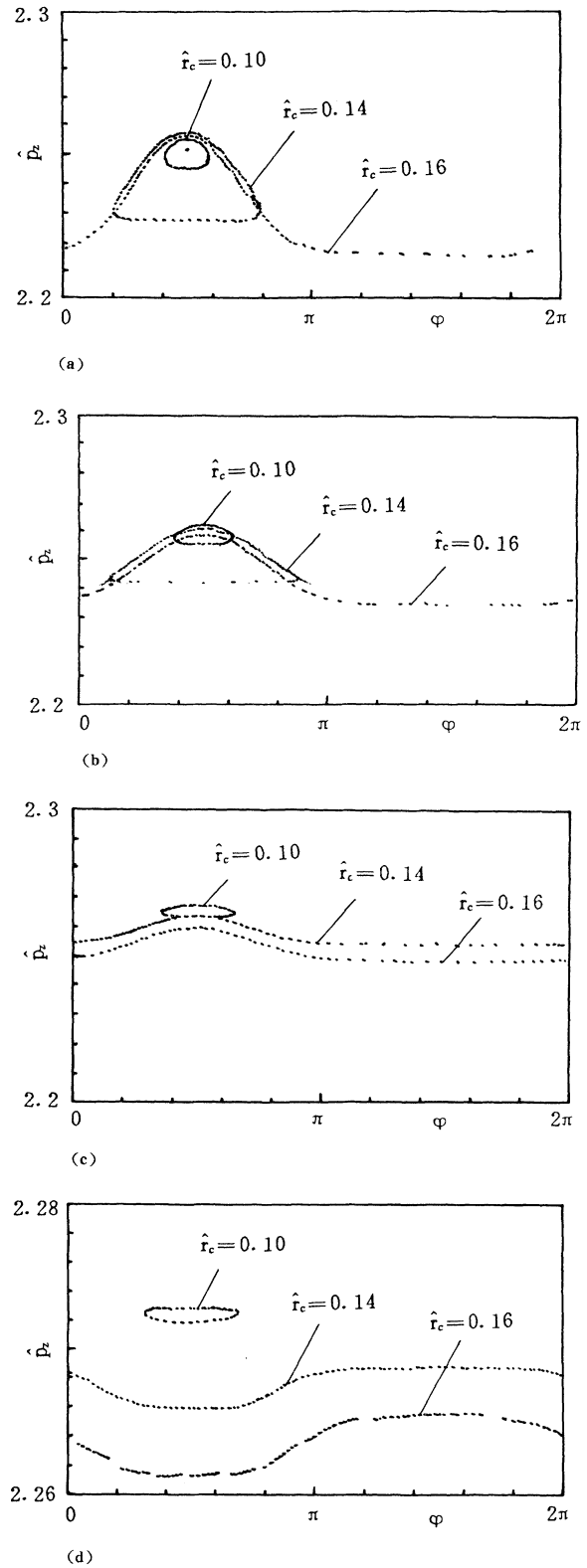


FIG. 3. Poincaré surface-of-section maps with  $\psi=0$ ,  $\text{mod}(2\pi)$ , where (a)  $\epsilon=0.00727$  ( $I_b=300$  A), (b)  $\epsilon=0.03635$  ( $I_b=1500$  A), (c)  $\epsilon=0.05453$  ( $I_b=2250$  A), and (d)  $\epsilon=0.07270$  ( $I_b=3000$  A), and other parameters are the same as those in Fig. 1.

to the beam spread so that their orbits were not helical. So it is necessary to analyze the influence of self-fields on Poincaré surface-of-section maps. Our numerical integration indicates that the fixed point is slightly influenced by the self-fields, but both the closed and open curves change with the increase of the self-fields.

To reduce the expense of calculations, we concentrate our attention on the three phase portraits with  $\hat{\tau}_c = 0.10, 0.14,$  and  $0.16$ . The situation for  $\epsilon = 0$  has been shown in Fig. 2, where the curve for  $\hat{\tau}_c = 0.16$  approximately is the separatrix, and the curves for  $\hat{\tau}_c = 0.10$  and  $0.14$  are closed. In Fig. 3(a), the self-field parameter  $\epsilon = 0.00727$  corresponds to the beam current  $I_b = 300$  A. The separatrix begins to become an open curve and to cross the curve of  $\hat{\tau}_c = 0.14$ . In Fig. 3(b) we let  $\epsilon = 0.03635$  ( $I_b = 1500$  A). The curve of  $\hat{\tau}_c = 0.14$  tends to be open and crosses the closed curve of  $\hat{\tau}_c = 0.10$ . When  $\epsilon = 0.05453$  ( $I_b = 2250$  A), we can see from Fig. 3(c) that the curve of  $\hat{\tau}_c = 0.14$  is entirely open, while the curve of  $\hat{\tau}_c = 0.16$  does not cross the curve of  $\hat{\tau}_c = 0.10$  again. In Fig. 3(d) the self-fields increase up to  $\epsilon = 0.07270$  ( $I_b = 3000$  A). We find that the curve of  $\hat{\tau}_c = 0.10$  remains closed and is no longer crossed by the curves of  $\hat{\tau}_c = 0.14$  and  $0.16$ . Compared with the situation of  $\epsilon = 0$ , the closed curve of  $\hat{\tau}_c = 0.10$  rises upon the curves of  $\hat{\tau}_c = 0.14$  and  $0.16$ , and the original hump becomes a valley. Figure 3 shows an interesting phenomenon: the variation range of the axial momentum of the equilibrium electrons has been compressed with the increase of beam current. This results in a reduction of the axial momentum spread. We guess that the beam quality may not degenerate even if the current increases up to 3000 A in experiment [12] with the limit of  $\hat{\tau}_c < 0.10$ .

## V. CONCLUSIONS

In this paper we have presented a comprehensive dynamics of the equilibrium electrons in a helical-wiggler free-electron laser with reversed guide magnetic field. Several conclusions can be drawn.

(1) The helical orbits are always stable and no longer divided into two groups as indicated in Ref. [14].

(2) There are four classes of phase curves without the self-fields taken into account: fixed point (corresponding to the helical orbits), closed phase curves (periodic orbits), open phase curves (nonperiodic orbits), and separatrix. The phase portrait is quite different from the one of the positive guide magnetic field: both closed and open phase curves lie on the same side of the separatrix.

(3) Some closed phase curves with relatively great gyroradius become open with the increase of the beam current, but the variation range of axial momentum is narrowed (which means reduction of the axial momentum spread).

(4) The quality of the electron beam in equilibrium may be improved by using a reversed guide magnetic field.

## ACKNOWLEDGMENT

This project was supported by the National Natural Science Foundation of China.

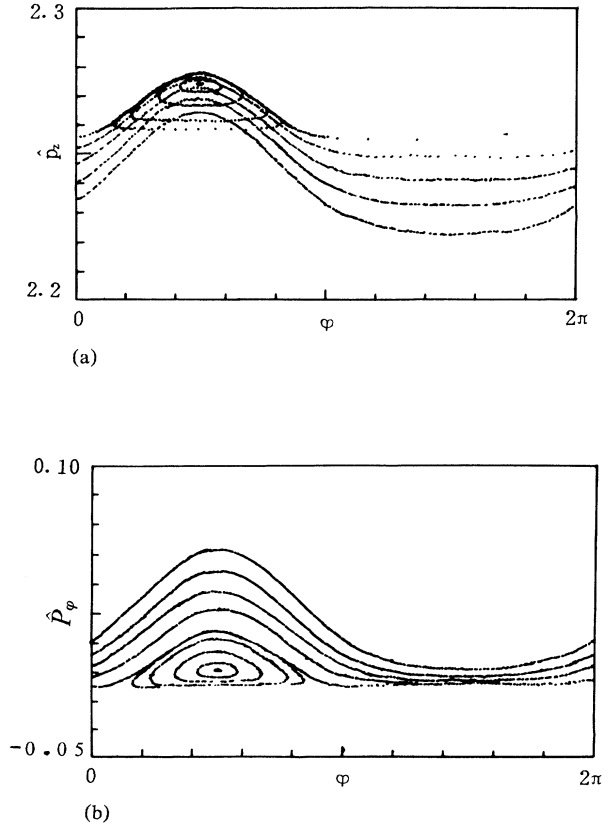


FIG. 4. The surface-of-section diagrams for  $\psi = 0, \text{mod}(2\pi)$  (a) in the  $\hat{p}_z$ - $\varphi$  plane, and (b) in the  $\hat{P}_\varphi$ - $\varphi$  plane, where  $\hat{\tau}_c = 0.074, 0.10, 0.12, 0.14, 0.16, 0.18, 0.20, 0.22,$  and  $0.24$ , and other parameters are the same as those in Fig. 2.

## APPENDIX

Strictly speaking, the phase plane for  $\psi = 0, \text{mod}(2\pi)$  should be formed by the variables  $\hat{P}_\varphi$  and  $\varphi$ , i.e., the  $\hat{P}_\varphi$ - $\varphi$  plane. Indeed, this surface-of-section map can be replaced by the  $\hat{p}_z$ - $\varphi$  plane with the aid of Eq. (25). Unlike the positive guide field, however, the reversed guide field results in an extraordinary view that the unboundary curves cross the closed curves in the  $\hat{p}_z$ - $\varphi$  plane. In order to show this character, we summarize Figs. 2(a), 2(b), and 2(c) as Fig. 4(a). Here one should be cautious not to make the misunderstanding that the phase trajectories in the  $\hat{P}_\varphi$ - $\varphi$  plane cross each other. In fact, the crosspoint in the  $\hat{p}_z$ - $\varphi$  plane does not correspond to the same values of  $\hat{P}_\varphi$  and  $\varphi$  for a fixed  $\hat{P}_\psi$  due to the different values of  $\hat{P}_z$  [see Eq. (25)]. That is to say, no crosspoint in the  $\hat{P}_\varphi$ - $\varphi$  plane corresponds to the crosspoint in the  $\hat{p}_z$ - $\varphi$  plane. As shown in Fig. 4(b), this explanation is verified by transforming the  $\hat{p}_z$ - $\varphi$  diagram to the  $\hat{P}_\varphi$ - $\varphi$  diagram. It is due to the practical meaning that  $\hat{p}_z$  represents the mechanical momentum in the axial direction that we prefer the  $\hat{p}_z$ - $\varphi$  diagram to the  $\hat{P}_\varphi$ - $\varphi$  diagram, as Chen and Davidson did in Ref. [6].

\*Address for correspondence.

†Permanent address: CAEP, P.O. Box 517, Chengdu, 610003, China

- [1] L. Frieland, *Phys. Fluids* **23**, 2376 (1980).
- [2] H. P. Freund, S. Johnston, and P. Sprangle, *IEEE J. Quantum Electron.* **QE-19**, 322 (1983).
- [3] S. C. Zhang and Z. Zhang, *Appl. Phys. Lett.* **55**, 1380 (1989).
- [4] S. C. Zhang and Z. Zhang, *Appl. Phys. Lett.* **57**, 837 (1990).
- [5] S. C. Zhang and Z. Zhang, *Int. J. Infrared Millimeter Waves* **9**, 1107 (1989).
- [6] C. Chen and R. C. Davidson, *Phys. Fluids B* **2**, 171 (1990).
- [7] C. Chen and R. C. Davidson, *Phys. Rev. A* **42**, 5041 (1990).
- [8] G. Spindler and G. Renz, *Phys. Fluids B* **3**, 3517 (1991).
- [9] G. Spindler and G. Renz, *Nucl. Instrum. Methods Phys. Res. A* **304**, 492 (1991).
- [10] L. Michel, A. Bourdier, and J. M. Buzzi, *Nucl. Instrum. Methods Phys. Res. A* **304**, 465 (1991).
- [11] S. C. Zhang and Y. Xu, *Phys. Lett. A* **179**, 311 (1993).
- [12] M. E. Conde and G. Bekefi, *Phys. Rev. Lett.* **67**, 3082 (1991).
- [13] K. R. Chu and A. T. Lin, *Phys. Rev. Lett.* **67**, 3235 (1991).
- [14] H. P. Freund and A. K. Ganguly, *IEEE Trans. Plasma Sci.* **PS-20**, 245 (1992).
- [15] G. Bekefi (private communication).
- [16] R. C. Davidson, *Theory of Nonneutral Plasma* (Addison-Wesley, Reading, MA, 1989).
- [17] J. Fajans, G. Bekefi, Y. Z. Yin, and B. Lax, *Phys. Fluids* **28**, 1995 (1985).